Available online at www.sciencedirect.com

ScienceDirect

Green Energy & Environment xxx (xxxx) xxx

www.keaipublishing.com/gee

Research paper

Mo/Fe bimetallic pyrophosphates derived from Prussian blue analogues for rapid electrocatalytic oxygen evolution

Jingyi Wang [a], Jiajia Huang [a,*], Siyu Zhao [b], Ivan P. Parkin [b], Zhihong Tian [d], Feili Lai [e], Tianxi Liu [f], Guanjie He [b,c,*]

[a] School of Chemical Engineering, Zhengzhou University, Zhengzhou, 450001, China
[b] Department of Chemistry, University College London, London, WC1H 0AJ, UK
[c] School of Chemistry, University of Lincoln, Joseph Banks Laboratories, Green Lane, Lincoln, LN6 7DL, UK
[d] Henan University, Jinming Avenue, Kaifeng, 475001, China
[e] Department of Chemistry, KU Leuven, Celestijnenlaan 200F, Leuven, 3001, Belgium
[f] Key Laboratory of Synthetic and Biological Colloids, Ministry of Education, School of Chemical and Material Engineering, International Joint Research Laboratory for Nano Energy Composites, Jiangnan University, Wuxi, 214122, China

Received 16 January 2022; revised 20 February 2022; accepted 27 February 2022
Available online ■ ■ ■

Abstract

Efficient and stable oxygen evolution electrocatalysts are indispensable for industrial applications of water splitting and hydrogen production. Herein, a simple and practical method was applied to fabricate (Mo, Fe)P_2O_7@NF electrocatalyst by directly growing Mo/Fe bimetallic pyrophosphate derived from Prussian blue analogues on three-dimensional porous current collector. In alkaline media, the developed material possesses good hydrophilic features and exhibits best-in-class oxygen evolution reaction (OER) performances. Surprisingly, the (Mo, Fe)P_2O_7@NF only requires overpotentials of 250 and 290 mV to deliver 100 and 600 mA cm^{-2} in 1 mol L^{-1} KOH, respectively. Furthermore, the (Mo, Fe)P_2O_7@NF shows outstanding performances in alkaline salty water and 1 mol L^{-1} high purity KOH. A worthwhile pathway is provided to combine bimetallic pyrophosphate with commercial Ni foam to form robust electrocatalysts for stable electrocatalytic OER, which has a positive impact on both hydrogen energy application and environmental restoration.

Keywords: Oxygen evolution reaction; Bimetallic pyrophosphate; Heterostructure; Self-supported electrocatalyst

1. Introduction

Hydrogen production by water electrolysis holds the advantages of clean, sustainability, high product purity and high conversion efficiency [1,2], which is crucial to the renewable-energy prospect [3–5]. Oxygen evolution reaction (OER) is a pivotal procedure on the rate of H_2 production in water splitting [6–9]. Owing to the multistep proton and electron transfer process, OER shows torpid kinetics compared with hydrogen evolution reaction (HER), which greatly impedes the overall water electrolysis [10–13]. Precious metals and their corresponding oxides are considered to be the most effective electrocatalysts over the past few years, while the scarcity and high costs inhibit their further practical application [14–17]. Therefore, extensive research has been committed to develop highly efficient transition metal-based electrocatalysts, for instance transition metal nitrides [18,19], carbides [20], phosphides [21], sulfide [22–24] and oxides [25], some of

* Corresponding authors. School of Chemical Engineering, Zhengzhou University, Zhengzhou, 450001, China
E-mail addresses: huangjiajia@zzu.edu.cn (J. Huang), g.he@ucl.ac.uk (G. He).

https://doi.org/10.1016/j.gee.2022.02.014

them can even surpass commercial noble metal electrocatalysts, *i.e.* ruthenium and iridium dioxides, which greatly accelerates the sluggish water splitting process.

As a type of coordination polymers composed of metal ions and ligands [26,27], Prussian blue analogues (PBAs) with inconstant metal compositions, uniform size and definite structures, are extensively employed as templates to fabricate nanostructured electrocatalysts [28]. In addition, the corresponding derivatives of PBAs (metal sulfides, hydroxides, and phosphates, *etc.*) also exhibit superb performances due to their high specific electrochemical surface area as well as superior electrical conductivity [29,30]. Among them, metal phosphates possess broad prospect as inexpensive and high efficiency OER electrocatalysts [31]. In particular, transition metal phosphates have ligand configuration and universal coordination geometry, which can not only adapt to the structural changes in the electrochemical processes, but also stabilize the states of the metal center in the intermediate [32]. In addition, the PO_4^{3-} group acts as a proton acceptor can promote the four-electron transfer process, which accounts for the special activity of the electrocatalyst [33]. Currently, further improving the activity of metal phosphate electrocatalysts has become a research focus [31,34]. Che et al. reported a layered metallic pyrophosphate [$K_2Co_3(P_2O_7)_2 \cdot 2H_2O$] with highly exposed surface area and special zigzag CoO_6 octahedral chains, which exhibited good electroactivity for OER with only a small overpotential of 296 mV to deliver 10 mA cm^{-2} [35]. Zhao et al. developed N-doped carbon coated bimetallic phosphates for effective water electrolysis, the overpotential of the optimal $(Fe_4Co_1)P_2O_7$@N-C is reduced by 100 mV compared to the uncoated counterparts and remains stable for 80 h at 40 mA cm^{-2} in alkaline medium [34]. As for the electrode design, three-dimensional (3D) structures were highlighted in recent years, PBA derivatives growing on 3D conductive substrate directly can further increase active sites for enlarge surface area and electrical conductivity [36], and Ni foam (NF) has a certain contribution to the performance of the electrocatalyst as current collector [37]. Self-supporting electrodes avoid the involvement of costly conductive polymeric binders and promote the stability of electrodes, which are beneficial to fast gas bubble releasing under large current density water splitting processes [38–40].

Since the restricted activity of single-component catalysts, the construction of heterogeneous nano catalysts has been confirmed to be operative to advance the catalytic activity [41]. Combining multiple components in a system stimulates the reconstruction of electronic structures, and the adsorption energy can be adjusted. Therefore, synergistic effects among multielement components can boost OER performances [42–44]. In our previous report, the synergistic effect between Mo and Fe species has been proven by computational study, which can promote incessant electron transfer between transition metal carbides and metal dopants, optimize active species and the carbon substrate could enhance the corrosion resistance of the catalyst [20]. Zhang et al. manufactured an innovative Co-Cu-Fe-Mo (oxy)hydroxide and verified advantages of designing multicomponent system and strongly synergistic effects of the elements in catalytic OER [45]. However, adopting bimetallic pyrophosphates for effectual electrochemical application was still seldom reported and the synthetic processes normally involved multi-steps.

Herein, a facile method was explored to prepare high efficiency OER electrocatalyst, Mo/Fe-PBA@NF are grown through a hydrothermal reaction where $K_4[Fe(CN)_6]$ is combined with the Mo salt. Mo/Fe-PBA@NF provides (Mo, Fe)P_2O_7@NF with desirable doping sources of Mo and Fe. After low-temperature phosphorizing in Ar, Mo/Fe bimetallic pyrophosphates (Mo, Fe)P_2O_7@NF can be synthesized. Contributing to abundant exposed surfaces, the construction of heterostructures and tight binding between active materials and conductive substrates, (Mo, Fe)P_2O_7@NF exhibits superior activity as OER electrocatalyst with an overpotential of 290 mV at 600 mA cm^{-2}. Furthermore, (Mo, Fe)P_2O_7@NF also shows outstanding performances in alkaline simulated seawater and high purity alkaline electrolyte at room temperature.

2. Experimental section

2.1. Preparation of samples

2.1.1. Preparation of Mo@NF

In the autoclave, $(NH_4)_6Mo_7O_{24} \cdot 4H_2O$ (0.16 mmol) and $Na_3C_6H_5O_7 \cdot 2H_2O$ (1.14 mmol) were dissolved into deionized water (30 mL), followed by the immersion of a clean Ni foam (2×4 cm^2). Subsequently, the autoclave was sealed and kept at 90 °C for 10 h. After cooling in the autoclave, the Mo@NF was obtained by washing with deionized water several times and then drying at 60 °C for 3 h in vacuum.

2.1.2. Preparation of Mo/Fe-PBA@NF

In the autoclave, $K_4[Fe(CN)_6]$ (0.31 mmol) was dissolved into deionized water (30 mL), followed by the immersion of a piece of Mo@NF. Subsequently, the autoclave was sealed and kept at 90 °C for 24 h. After cooling in the autoclave, the Mo/Fe-PBA@NF was obtained by washing with deionized water several times and then drying at 60 °C for 3 h in vacuum.

2.1.3. Preparation of (Mo, Fe)P_2O_7@NF

An appropriate amount of Mo/Fe-PBA@NF was placed in a porcelain boat, and then transferred to the center of the tube furnace. Then the sodium hypophosphate monohydrate (200 mg) was placed upstream of the furnace. Subsequently, the furnace was kept at 350 °C for 3 h under nitrogen flow. The (Mo, Fe)P_2O_7@NF area mass loading was calculated to be 1.2 mg cm^{-2}.

2.1.4. Preparation of P-Mo@NF-1

The synthesis method is the same as (Mo, Fe)P_2O_7@NF, except that the step of reacting the sample with $K_4[Fe(CN)_6]$ solution is omitted.

2.1.5. Preparation of P-Mo@NF-2

The synthesis method is the same as P-Mo@NF-1, except that the $(NH_4)_6Mo_7O_{24} \cdot 4H_2O$ (0.16 mmol) and

Please cite this article as: J. Wang et al., Mo/Fe bimetallic pyrophosphates derived from Prussian blue analogues for rapid electrocatalytic oxygen evolution, Green Energy & Environment, https://doi.org/10.1016/j.gee.2022.02.014

$Na_3C_6H_5O_7 \cdot 2H_2O$ (1.14 mmol) is replaced by $(NH_4)_6Mo_7O_{24} \cdot 4H_2O$ (0.16 mmol).

2.1.6. Preparation of P-Fe-PBA@NF

The synthesis method is the same as (Mo, Fe)P_2O_7@NF, except that the step of reacting the sample with $(NH_4)_6Mo_7O_{24} \cdot 4H_2O$ (0.16 mmol) and $Na_3C_6H_5O_7 \cdot 2H_2O$ (1.14 mmol) mixed solution is omitted.

2.2. Electrochemical measurements

The entire electrochemical test was carried out by CHI 660E electrochemical workstation with a three-electrode system. The as-prepared samples, saturated Ag/AgCl electrode and graphite rod serve as the working electrode, reference electrode and counter electrode, respectively, and 1 mol L^{-1} KOH (purity: 85%), 1 mol L^{-1} KOH (purity: 85%) with 0.5 mol L^{-1} NaCl added, 1 mol L^{-1} KOH (purity: 85%) with 1 mol L^{-1} NaCl added, and 1 mol L^{-1} KOH (purity: 99.99%) as electrolytes, which the pH were all about 14. The polarization curves were measured at a scan rate of 5 mV s^{-1}. The electrochemically active surface area (ECSA) was assessed by surveying the double layer capacitance (C_{dl}) from testing cyclic voltammetry (CV) at different scan rates in the voltage window of −0.45 ~ −0.35 V (*vs.* Ag/AgCl). The slope according to the plotting the differences of charging current density ($\Delta J = J_a - J_c$) at the potential of −0.4 V versus the scan rates represents twice of C_{dl}. Electrochemical impedance spectra (EIS) were obtained at a 5-mV amplitude over the frequency range of 100 kHz to 0.1 Hz.

2.3. Characterization

Scanning electron microscope (SEM) was conducted on Zeiss Merlin Compact. Transmission electron microscopy (TEM) and high-resolution TEM (HRTEM) were collected on FEI TalosF200S. Prior to the testing, TEM specimen was dispersed in absolute ethyl alcohol and sonicated for 2 h. The crystallinity of products was detected by X-ray diffraction (XRD) on an X-ray diffractometer with Cu Kα radiation (Bruker D8 Advance). X-ray photoelectron spectroscopy (XPS) were carried out on Thermo Electron ESCALAB 250 instruments. Brunauer-Emmett-Teller (BET) surface area measurements were collected using a Micromeritics ASAP2460 with nitrogen adsorption at 77k.

3. Results and discussion

3.1. The compositional and structural characterization for (Mo, Fe)P_2O_7@NF

Due to 3D microporous feature and ultra-high electrical conductivity, the cost-effective commercial NF was employed for dispersing active species as a supporting substrate. The (Mo, Fe)P_2O_7@NF was synthesized by a two-step hydrothermal method and low-temperature phosphating (Fig. 1(a)). The synthetic details are provided in experimental section. Since the electronegativity of Fe is stronger than that of Mo, it is easier for Fe to combine with P, which would induce the generation of $MoP_2O_7/Fe_2P_2O_7$ heterostructures during the reaction. The pore size of (Mo, Fe)P_2O_7@NF is ranging from 100 to 800 μm, which is consistent with the macroporous structure of the 3D NF (Fig. S1). The self-supported (Mo, Fe)P_2O_7@NF electrocatalyst was directly used as work electrode. In virtue of the multicomponent architecture, the unique design method bestows the $MoP_2O_7/Fe_2P_2O_7$ electrocatalyst with multiple advantages: i) the in-situ growth structure allows for rapid electron transfer and excellent electrical conductivity that can assurance the structural stability of the composite; ii) the formed $MoP_2O_7/Fe_2P_2O_7$ heterostructure could boost additional charge transfer to expedite the reaction kinetics profited from the build-in electric field effect; iii) the strong hydrophilic surface produced in (Mo, Fe)P_2O_7@NF accelerates the electrolyte diffusion and inhibits the retention of bubbles on the electrode surface. Consequently, (Mo, Fe)P_2O_7@NF composite could exhibit remarkable durability and outstanding catalytic activity when used as electrode for OER.

We first examined the surface morphology of (Mo, Fe)P_2O_7@NF by SEM. Fig. 1(b) shows the SEM image of Mo@NF, a few pores on the surface of Mo@NF are obvious after the first hydrothermal reaction. From the SEM image of Mo/Fe-PBA@NF in Fig. 1(c), it can be observed that the NF surface becomes rougher and the pores increase. As shown in Fig. 1(d), the reacted NF is evenly coated by uniformly distributed nanoparticles of (Mo, Fe)P_2O_7@NF. The high-magnification SEM image and TEM image in Figs. 1(e) and 2(a) reveal that gullies between the nano blocks are several nanometers in size and generate the thin edges of nanoparticles, which may offer diffusible channels for the electrolyte. The HRTEM image of (Mo, Fe)P_2O_7@NF (Fig. 2(b)) shows that rich crystalline-amorphous boundaries are generated by the crystalline and amorphous parts, which may deliver more electrocatalytically active sites [46]. The nanoparticles are surrounded by amorphous carbon, which makes for improving the electrical conductivity of the entire system [47–49]. The crystalline part of Fig. 2(c) shows the legible lattice fringe with a spacing of 2.9 Å is vested in the (022) crystal plane of $Fe_2P_2O_7$ and the lattice fringe with a distance of 3.2 Å is indexed to the (211) lattice plane of MoP_2O_7. The selected area electron diffraction pattern (SAED) in Fig. 2(d) displays definite diffraction rings, which are ascribed to the (022) and (32−1) planes of $Fe_2P_2O_7$ and the (311), (331) and (420) planes of MoP_2O_7. Moreover, the scanning TEM and corresponding energy dispersive X-ray spectroscopy elemental mapping images of (Mo, Fe)P_2O_7@NF in Fig. 2(e) verify the evenly distribution of Mo, Fe, P, O, C and N in the nanostructures, Ni is obviously only present on the surface of the nanoparticles and not inside, which exists may due to the ultrasonic peeling from the NF.

The crystalline phase of (Mo, Fe)P_2O_7@NF was identified by XRD patterns (Fig. 3(a)), the three strongest peaks come from the original NF, and the other peaks are well pointed to $Fe_2P_2O_7 \cdot 2H_2O$ (PDF# 50-1798) and MoP_2O_7 (PDF# 39-

Please cite this article as: J. Wang et al., Mo/Fe bimetallic pyrophosphates derived from Prussian blue analogues for rapid electrocatalytic oxygen evolution, Green Energy & Environment, https://doi.org/10.1016/j.gee.2022.02.014

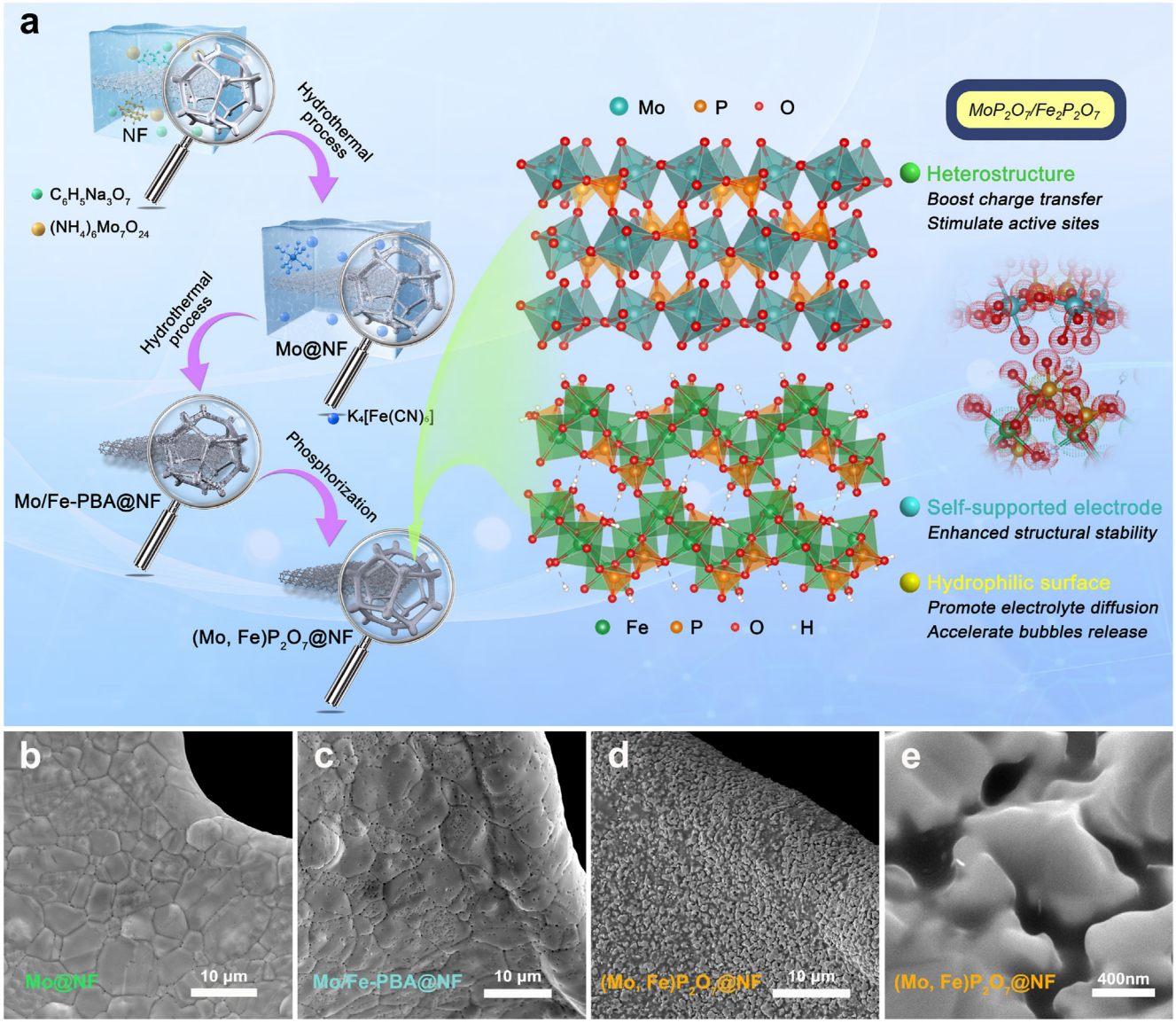

Fig. 1. Schematic diagram of synthetic routes for (Mo, Fe)P_2O_7@NF (a). SEM images of Mo@NF (b), Mo/Fe-PBA@NF (c), (Mo, Fe)P_2O_7@NF (d), and a zoom-in of (Mo, Fe)P_2O_7@NF (e).

0026), which align with the SAED patterns (Fig. 2(d)). Meanwhile, XPS was applied to detect the components and elemental valence states of (Mo, Fe)P_2O_7@NF. In Fig. 3(b), the characteristic peaks of Mo, Fe, P, Ni, C, and O can be observed in the NF after surface treatment, verify the coexistence of these elements. Fig. 3(c) shows the Ni 2*p* spectrum, in which spin-orbit peaks at 856.1 eV (Ni $2p_{3/2}$) and 874.1 eV (Ni $2p_{1/2}$) in consort with satellite peaks (labeled as "Sat.") stand for the oxidation state of Ni^{2+}, and the peaks at 858.6 eV and 877.6 eV belong to Ni^{3+} [50]. With reference to the Ni 2*p* XPS spectrum of pure NF (Fig. S2), the two peaks at 851.9 and 869.2 eV correspond to Ni^0, (852.1 eV and 869.5 eV for pure NF). The C 1*s* spectrum of (Mo, Fe)P_2O_7@NF exhibits peaks at 284.7, 285.8 and 288.5 eV, which could assign to the C-C, C-N, and C-O bonds, respectively (Fig. S3) [51–54]. The N 1*s* spectrum displays peaks at 398.6 and 399.9 eV, which belong to pyridinic-N and pyrrolic-N, respectively (Fig. S4). Fig. 3(d) displays the Mo 3*d* spectrum, in which the peaks at 234.1 and 236.2 eV are originated from Mo^{6+}, and the peaks at 229.5 and 233.3 eV attributed to Mo^{4+}, respectively [55,56], indicating the presence of Mo-P and the oxidation state of Mo. In the Fe 2*p* XPS spectrum (Fig. 3(e)), there are three peaks which at 705.7 eV/712.1 eV for Fe $2p_{3/2}$ and 723.5 eV for Fe $2p_{1/2}$, representing Fe^{2+} and Fe-P exist, respectively [57]. Transition metal sites with high valence states have been proved to speed up the kinetics of the reaction, and thus provide highly intrinsic activity [58]. The P 2*p* spectrum exhibits one typical peak locate at 133.4 eV is attributed to the oxidized metal phosphate of (Mo, Fe)P_2O_7@NF (Fig. 3(f)). Another peak at 129.3 eV

Please cite this article as: J. Wang et al., Mo/Fe bimetallic pyrophosphates derived from Prussian blue analogues for rapid electrocatalytic oxygen evolution, Green Energy & Environment, https://doi.org/10.1016/j.gee.2022.02.014

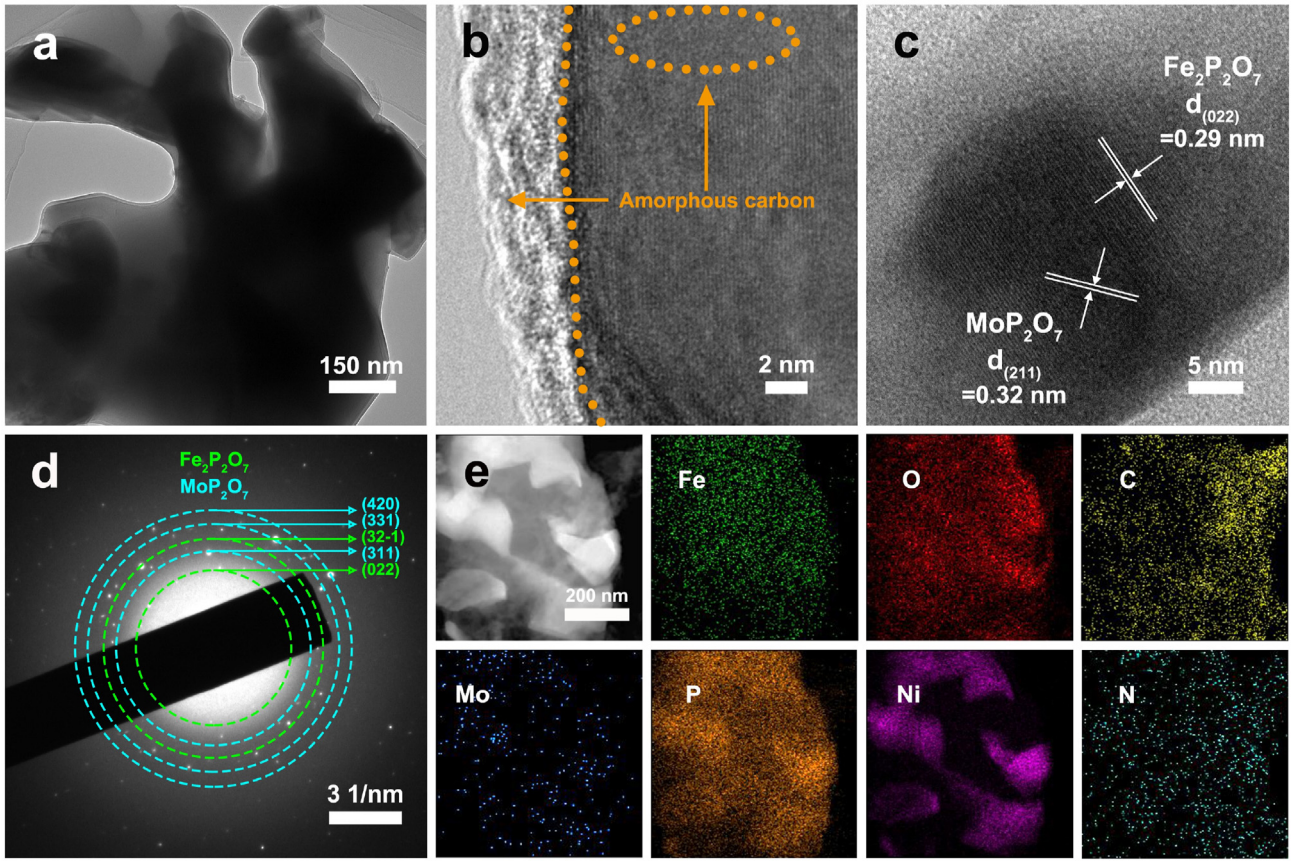

Fig. 2. (a) TEM, (b, c) HRTEM images, (d) SAED pattern and (e) corresponding elemental mapping of Mo, Fe, P, O, Ni, C and N for (Mo, Fe)P_2O_7@NF.

corresponds to the representative signal of metal phosphides. Therefore, this method efficiently coats the NF surface with Mo/Fe bimetallic pyrophosphates.

3.2. Electrochemical activity and stability for (Mo, Fe) P_2O_7@NF

The OER performance of the above electrocatalysts were estimated in 1 mol L^{-1} KOH firstly (purity: 85%). IrO_2 powders were used as advanced OER electrocatalysts for comparison. All initial electrochemical data has been applied an *i*R compensation. The OER polarization curves displayed inFig. 4(a), compared with pure NF and Mo/Fe-PBA@NF, (Mo, Fe)P_2O_7@NF shows a significant improvement of OER electrocatalytic performance, which is even better than the commercial IrO_2 benchmark. The required overpotentials (η) for (Mo, Fe)P_2O_7@NF to provide 10 and 100 mA cm^{-2} are 130 and 250 mV, respectively, which are far better than pure NF (309 and 370 mV), Mo/Fe-PBA@NF (184 and 332 mV) and IrO_2 (257 and 322 mV). Moreover, (Mo, Fe)P_2O_7@NF displays promising activity with 600 mA cm^{-2} under 290 mV, which is approximately 14 times compared to IrO_2, representing extra high electrocatalytic activity.

In addition, as Fig. 4(b), (Mo, Fe)P_2O_7@NF displays a smaller Tafel slope of 40 mV dec^{-1} compared to IrO_2 (72 mV dec^{-1}), testifies a more rapid electrocatalytic kinetics. The ECSA determined by estimating C_{dl} with CV tests (Fig. S5) confirmed that the bimetallic active center excited more active sites [59]. Furthermore, the C_{dl} value obviously rises after phosphating (Fig. 4(c)). The C_{dl} value of (Mo, Fe)P_2O_7@NF (12.3 mF cm^{-2}) is 1.7 times compared to the Mo/Fe-PBA@NF (7.2 mF cm^{-2}), signifying more favourable active area and available active sites. As shown in Fig. S6, the specific surface area of (Mo, Fe)P_2O_7@NF (13.06 m^2 g^{-1}) is also higher than pure Ni foam (5.49 m^2 g^{-1}), which specifies that roughening the originally surface with uneven particles is effective and makes for enlarging accessible surface areas. Moreover, (Mo, Fe)P_2O_7@NF exhibits a favorable hydrophilic feature (Fig. S7a) contrasted to NF with the hydrophobic surface (Fig. S7b), which not only contributes to electrolyte to contact the electrode but also benefits the quick release of bubbles. The super-hydrophilic surface is another key factor for the obviously promoted electrochemical catalytic activity of (Mo, Fe)P_2O_7@NF at large current densities [60,61]. Nyquist plots in Fig. 4(d) recorded by EIS (the inset is equivalent circuit) further shows that (Mo, Fe)P_2O_7@NF possesses tiny charge-transfer resistance (R_{ct}) compared to Mo/Fe-PBA@NF and commercial NF, and (Mo, Fe)P_2O_7@NF reveals the minimum R_{ct} value of 1.36 Ω, indicating the effective charge-transport ability with promising electrocatalytic dynamics [62]. Furthermore, the activity of (Mo, Fe)P_2O_7@NF could be maintained with only a negligible loss

Please cite this article as: J. Wang et al., Mo/Fe bimetallic pyrophosphates derived from Prussian blue analogues for rapid electrocatalytic oxygen evolution, Green Energy & Environment, https://doi.org/10.1016/j.gee.2022.02.014

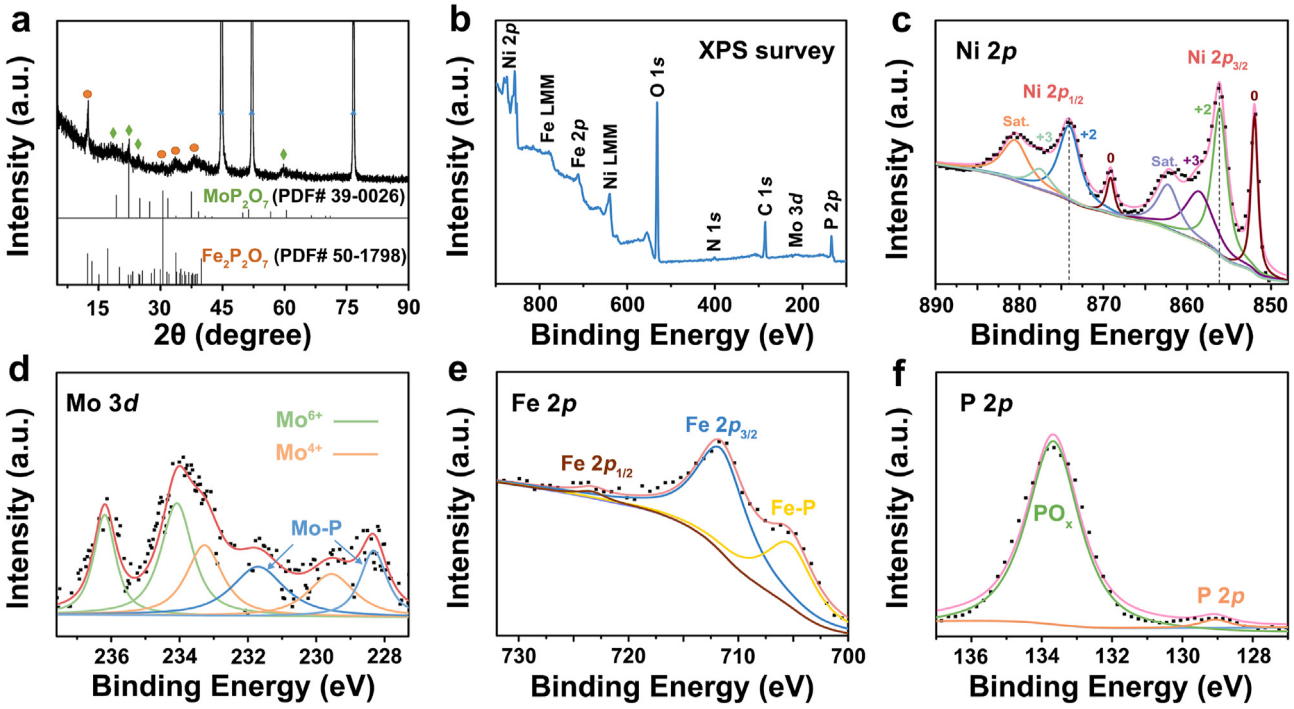

Fig. 3. (a) XRD pattern, (b) XPS survey, and (c) Ni 2*p*, (d) Mo 3*d*, (e) Fe 2*p* and (f) P 2*p* high-resolution XPS spectra for (Mo, Fe)P_2O_7@NF.

after 10,000 CV scans in 1 mol L^{-1} KOH (Fig. 4(e)). Control experiments further validate that the appropriate amount of phosphorus source has significant effect in enhancing the electrochemistry activity of the electrocatalyst. As shown in Fig. S8, 0.2 g of the P source maximizes the activity of the electrocatalyst. Also shown in Fig. S9, comparative experiments prove the necessity of bimetal active centers. The synthetic details of P-Mo@NF-1, P-Mo@NF-2, P-Fe-PBA@NF are provided in the experimental section. Compared with the single metal catalyst above, the activity of (Mo, Fe)P_2O_7@NF with bimetal active centers has significant advantage.

Based on the advantages of seawater electrolysis that can simultaneously perform hydrogen production and seawater desalination [63,64], the OER performance of (Mo, Fe)P_2O_7@NF was then assessed in basic simulated seawater electrolytes (1 mol L^{-1} KOH with 0.5 mol L^{-1} NaCl added and 1 mol L^{-1} NaCl added) to evaluate the chlorine corrosion resistance of (Mo, Fe)P_2O_7@NF. As illustrated inFig. 4(f), the performance of (Mo, Fe)P_2O_7@NF in two simulated seawater electrolytes remains remarkable, the required overpotentials to reach 500 mA cm^{-2} are 354 and 337 mV, respectively, the performance is close to that in 1 mol L^{-1} KOH in either of these electrolytes. Moreover, the required overpotential to achieve 600 mA cm^{-2} is much less than that for initiating the oxidation of chloride to hypochlorite (490 mV), indicating the corrosion of Cl^- has little effect on (Mo, Fe)P_2O_7@NF [64,65]. In the high purity KOH electrolyte (1 mol L^{-1}, purity: 99.99%), (Mo, Fe)P_2O_7@NF exhibits small activity decay due to the lack of dynamic active sites formed by trace elements (such as Fe, Mn, etc., which have been proven to be beneficial to OER) between the electrolyte and the electrode. In 1 mol L^{-1} KOH (purity: 85%), it is precisely owing to these trace elements that moved between the electrode and the electrolyte to form a dynamic balance so as to increase the electrocatalytic activity [66]. In this situation, the required overpotentials of (Mo, Fe)P_2O_7@NF to deliver 100 and 500 mA cm^{-2} are still 319 and 379 mV, respectively. Another vital index for assessing the performance of an electrocatalyst is the electrochemical stability. We then explored the stability of (Mo, Fe)P_2O_7@NF through long-term durability tests under a fixed overpotential in different electrolytes. Chronopotentiometric tests in Fig. 4(g) further reflected that (Mo, Fe)P_2O_7@NF remained almost steady at 100 mA cm^{-2} over 89 h in 1 mol L^{-1} KOH (purity: 85%) and 1 mol L^{-1} KOH (purity: 85%) with 1 mol L^{-1} NaCl added, with the relative decrements of current density are 3% and 9%, which is 13% in 1 mol L^{-1} KOH (purity: 99.99%) at 150 mA cm^{-2} over 49 h. After long time test, the pH of electrolyte is basically stable, changing from 13.85 to 13.63. The real-time current density remains steady with a negligible decrease throughout the uninterrupted operation in alkaline electrolytes, demonstrating its outstanding OER durability, which largely roots in the robust connection between the bimetallic active centers and the NF. Meanwhile, the XPS spectra after the OER tests display that the binding energies of Ni 2*p* and Fe 2*p* shift slightly to higher binding energy regions, and the peak of Ni^0 noticeably reduces and even disappears, which illustrate the formation of metal oxide/hydroxide species during the OER process [67,68]. The binding energies of Mo 3*d* and P 2*p* barely change before and after OER tests, indicating that Mo and P species remained stable without further oxidation in the OER process (Fig. S10). Impressively, the low voltage is compared favorably with the values obtained on most of PBA-based and self-supported

Please cite this article as: J. Wang et al., Mo/Fe bimetallic pyrophosphates derived from Prussian blue analogues for rapid electrocatalytic oxygen evolution, Green Energy & Environment, https://doi.org/10.1016/j.gee.2022.02.014

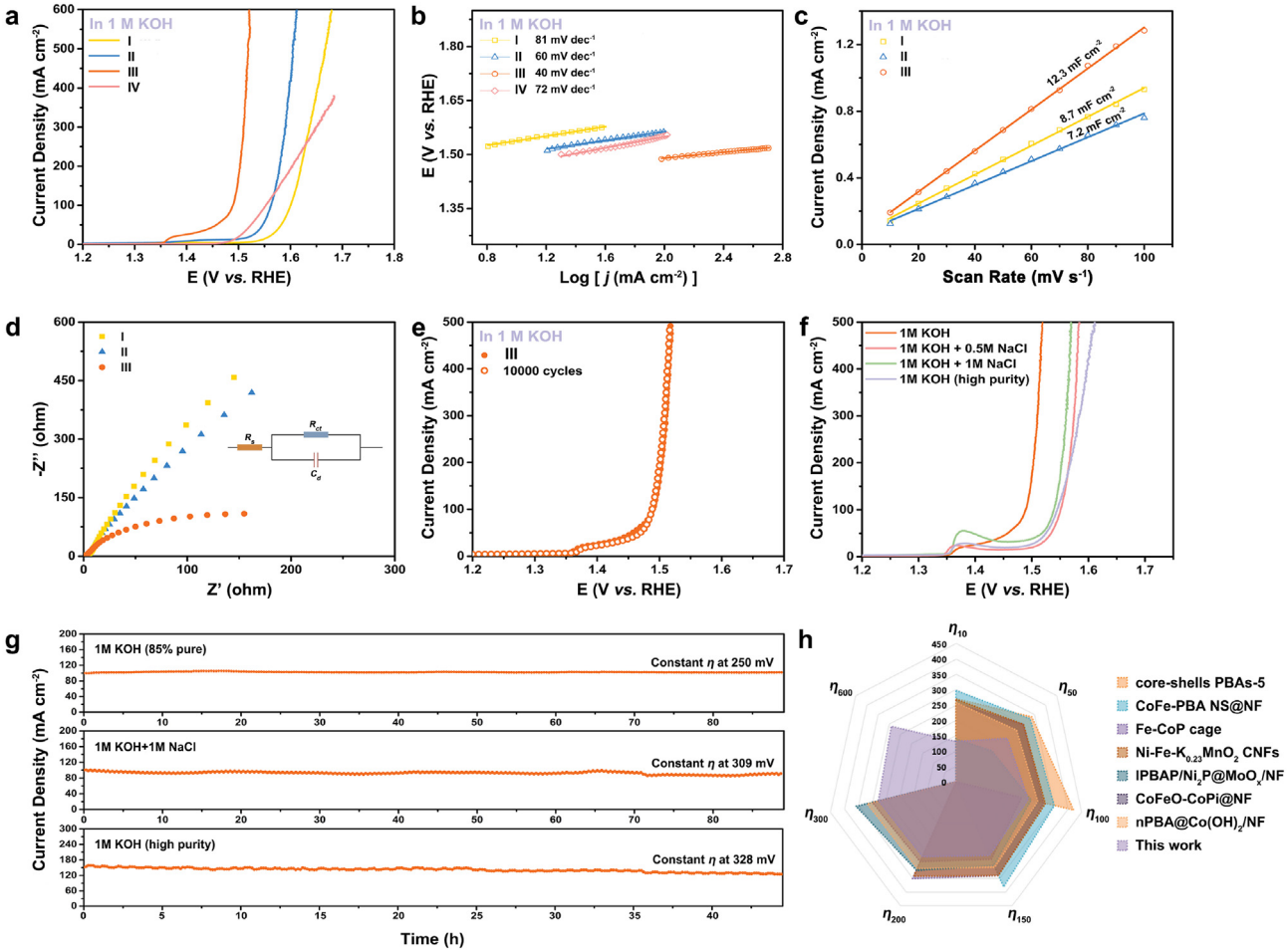

Fig. 4. (a) Polarization curves after *i*R-corrected with a scan rate of 5 mV s^{-1} and (b) corresponding Tafel slopes of (I): pure NF, (II): Mo/Fe-PBA@NF, (III): (Mo, Fe)P_2O_7@NF, (IV): IrO_2 (Ir: 84.5%) in 1 mol L^{-1} KOH (purity: 85%). (c) The fitting of C_{dl} and (d) EIS Nyquist plots of I, II and III. The inset in (d) shows the equivalent circuit. (e) Polarization curves after *i*R-corrected of III initially and after 10,000 cycles in 1 mol L^{-1} KOH (purity: 85%). (f) Polarization curves tested in different electrolytes. (g) Chronoamperometry curves at $\eta = 250$ mV in 1 mol L^{-1} KOH (purity: 85%), at $\eta = 309$ mV in 1 mol L^{-1} KOH (purity: 85%) with 0.5 mol L^{-1} NaCl added and at $\eta = 328$ mV in 1 mol L^{-1} KOH (purity: 99.99%). (h) Comparison of OER performance of (Mo, Fe)P_2O_7@NF with other PBA-based electrocatalysts.

electrocatalysts, i.e., core-shell PBAs-5 [69], CoFe-PBA NS@NF [70], Fe-CoP cage [71], Ni-Fe-$K_{0.23}MnO_2$ CNFs [72], IPBAP/Ni_2P@MoO_x/NF [73], CoFeO-CoPi@NF [74], and nPBA@$Co(OH)_2$/NF [75] (See comparison details in Fig. 4(h)).

4. Conclusions

In summary, we have demonstrated that Mo/Fe bimetallic pyrophosphate MoP_2O_7 and $Fe_2P_2O_7$ can be approved as highly efficient OER electrocatalysts. Profit from the advantages of heterogeneous structure activation of rich active sites, hydrophilic feature, smaller charge-transfer resistance, self-supporting electrode configuration, (Mo, Fe)P_2O_7@NF exhibits noticeable OER electrocatalytic activity with the low required overpotentials of 250 and 290 mV to deliver 100 and 600 mA cm^{-2} current densities in 1 mol L^{-1} KOH (purity: 85%), respectively, and outstanding activity and stability in basic salty water and 1 mol L^{-1} high purity KOH. This study offers a new approach for developing efficient and cost-cutting electrocatalysts for OER, and provides an effective and novel method for designing self-supported electrodes to achieve the industrial current density (>500 mA cm^{-2}) at low overpotentials for OER.

Declaration of competing interest

The authors declared no conflicts of interests.

Acknowledgements

This work was supported by National Natural Science Foundation of China (No. 51873198), the Engineering and Physical Sciences Research Council (EPSRC, EP/V027433/1), and the Royal Society (RGS\R1\211080).

Appendix A. Supplementary data

Supplementary data to this article can be found online at https://doi.org/10.1016/j.gee.2022.02.014.

References

[1] X.Y. Yu, Y. Feng, B.Y. Guan, X.W. Lou, U. Paik, Energy Environ. Sci. 9 (2016) 1246–1250.
[2] S. Anantharaj, V. Aravindan, Adv. Energy Mater. 10 (2020) 30.
[3] B. Wang, C. Tang, H.F. Wang, X. Chen, R. Cao, Q. Zhang, Adv. Mater. 31 (2019) e1805658.
[4] Z. Pu, J. Zhao, I.S. Amiinu, W. Li, M. Wang, D. He, S. Mu, Energy Environ. Sci. 12 (2019) 952–957.
[5] X. Tian, P. Zhao, W. Sheng, Adv. Mater. 31 (2019) e1808066.
[6] S. Jo, S. Noh, K.R. Wee, J.H. Shim, ChemElectroChem 7 (2020) 3725–3732.
[7] Y. Gorlin, T.F. Jaramillo, J. Am. Chem. Soc. 132 (2010) 13612–13614.
[8] F.Y. Cheng, J. Chen, Chem. Soc. Rev. 41 (2012) 2172–2192.
[9] A.J. Bard, M.A. Fox, Accounts Chem. Res. 28 (1995) 141–145.
[10] S. Lei, Q.H. Li, Y. Kang, Z.G. Gu, J. Zhang, Appl. Catal. B Environ. 245 (2019) 1–9.
[11] M. Kunitski, N. Eicke, P. Huber, J. Köhler, S. Zeller, J. Voigtsberger, N. Schlott, K. Henrichs, H. Sann, F. Trinter, L.P.H. Schmidt, A. Kalinin, M.S. Schöffler, T. Jahnke, M. Lein, R. Dörner, Nat. Commun. 10 (2019) 1–7.
[12] Q. Shi, C. Zhu, D. Du, Y. Lin, Chem. Soc. Rev. 48 (2019) 3181–3192.
[13] L. Yu, H. Zhou, J. Sun, I.K. Mishra, D. Luo, F. Yu, Y. Yu, S. Chen, Z. Ren, J. Mater. Chem. A 6 (2018) 13619–13623.
[14] J.T. Ren, Y.L. Yao, Z.Y. Yuan, Green Energy Environ. 6 (2021) 620–643.
[15] M.F. Li, K. Duanmu, C.Z. Wan, T. Cheng, L. Zhang, S. Dai, W.X. Chen, Z.P. Zhao, P. Li, H.L. Fei, Y.M. Zhu, R. Yu, J. Luo, K.T. Zang, Z.Y. Lin, M.N. Ding, J. Huang, H.T. Sun, J.H. Guo, X.Q. Pan, W.A. Goddard III, P. Sautet, Y. Huang, X.F. Duan, Nat. Catal. 2 (2019) 495–503.
[16] S.Q. Zhou, L. Shang, Y.X. Zhao, R. Shi, G.I.N. Waterhouse, Y.C. Huang, L.R. Zheng, T.R. Zhang, Adv. Mater. 31 (2019) 1900509.
[17] L.C. Seitz, C.F. Dickens, K. Nishio, Y. Hikita, J. Montoya, A. Doyle, C. Kirk, A. Vojvodic, H.Y. Hwang, J.K. Norskov, T.F. Jaramillo, Science 353 (2016) 1011–1014.
[18] R. Zeng, Y. Yang, X.R. Feng, H.Q. Li, L.M. Gibbs, F.J. Disalvo, H.D. Abruña, Sci. Adv. 8 (2022) eabj1584.
[19] Y.K. Lu, Z.X. Li, Y.L. Xu, L.Q. Tang, S.J. Xu, D. Li, J.J. Zhu, D.L. Jiang, Chem. Eng. J. 411 (2021) 128433.
[20] J. Huang, J. Wang, R. Xie, Z. Tian, G. Chai, Y. Zhang, F. Lai, G. He, C. Liu, T. Liu, P.R. Shearing, D.J.L. Brett, J. Mater. Chem. A 8 (2020) 19879–19886.
[21] S.Y. Zhao, R.K. Xie, L.Q. Kang, M.N. Yang, X.Y. He, W.Y. Li, R. Wang, D.J.L. Brett, G.J. He, G.L. Chai, I.P. Parkin, Small Sci 1 (2021) 2100032.
[22] S.Y. Zhao, M.N. Yang, Y.S. Tan, D.J.L. Brett, G.J. He, I.P. Parkin, Multifunct. Mater. 4 (2021) 25001.
[23] J.J. Duan, Z. Han, R.L. Zhang, J.J. Feng, L. Zhang, Q.L. Zhang, A.J. Wang, J. Colloid Interface Sci. 588 (2021) 248–256.
[24] H. Zhang, J. Wang, Q. Cheng, P. Saha, H. Jiang, Green Energy Environ. 5 (2020) 492–498.
[25] Z. Guo, Y.Y. Pang, H. Xie, G.J. He, I.P. Parkin, G.L. Chai, ChemElectroChem. 8 (2021) 135–141.
[26] S. Kitagawa, R. Kitaura, S.i. Noro, Angew. Chem. Int. Ed. 43 (2004) 2334–2375.
[27] A.A. Karyakin, Electroanalysis 13 (2001) 813–819.
[28] J. Nai, X.W. Lou, Adv. Mater. 31 (2019) 1706825.
[29] Y.X. Yang, B.L. Li, Q. Zhang, W.H. Guo, X.H. Wang, L.J. Li, H.Q. Luo, N.B. Li, Energy Technol. 9 (2021) 2000178.
[30] L. Zhang, Y.T. Ma, J.J. Duan, Y.Q. Yao, J.J. Feng, A.J. Wang, J. Colloid Interface Sci. 611 (2022) 205–214.
[31] Y. Krishnan, S. Bandaru, N.J. English, Catal. Sci. Technol. 11 (2021) 4619–4626.
[32] J. Wang, H.C. Zengg, ACS Appl. Mater. Interfaces 10 (2018) 6288–6298.
[33] M.W. Kanan, Y. Surendranath, D.G. Nocera, Chem. Soc. Rev. 38 (2009) 109–114.
[34] D. Zhao, Q. Shao, Y. Zhang, X. Huang, Nanoscale 10 (2018) 22787–22791.
[35] Q. Che, Q. Ma, J. Wang, Y. Zhu, R. Shi, P. Yang, Mater. Lett. 272 (2020) 127877.
[36] H.F. Shi, Q.Q. Zha, Y.H. Ni, J. Alloys Compd. 904 (2022) 164052.
[37] S. Riyajuddin, K. Azmi, M. Pahuja, S. Kumar, T. Maruyama, C. Bera, K. Ghosh, ACS Nano 15 (2021) 5586–5599.
[38] Y.S. Tan, R.K. Xie, S.Y. Zhao, X.K. Lu, L.X. Liu, F.J. Zhao, C.Z. Li, H. Jiang, G.L. Chai, D.J.L. Brett, P.R. Shearing, G.J. He, I.P. Parkin, Adv. Funct. Mater. 31 (2021) 2105579.
[39] Y. Bai, L.C. Zhang, Q.L. Li, Y.K. Wu, Y.P. Wang, M.W. Xu, S.J. Bao, ACS Sustain. Chem. Eng. 9 (2021) 1297–1303.
[40] H. Sun, Z. Yan, F. Liu, W. Xu, F. Cheng, J. Chen, Adv. Mater. 32 (2020) 1806326.
[41] H.S. Jiang, K.N. Zhang, W.Y. Li, Z. Cui, S.A. He, S.Y. Zhao, J. Li, G.J. He, P.R. Shearing, D.J.L. Brett, J. Power Sources 472 (2020) 228497.
[42] X.Q. Ye, J.C. Fan, Y.L. Min, P.H. Shi, Q.J. Xu, Nanoscale 13 (2021) 14854–14865.
[43] M.P. Chen, D. Liu, B.Y. Zi, Y.Y. Chen, D. Liu, X.Y. Du, F.F. Li, P.F. Zhou, Y. Ke, J.L. Li, K.H. Lo, C.T. Kwok, W.F. Ip, S. Chen, S.P. Wang, Q.J. Liu, H. Pan, J. Energy Chem. 65 (2022) 405–414.
[44] J.J. Duan, R.L. Zhang, J.J. Feng, L. Zhang, Q.L. Zhang, A.J. Wang, J. Colloid Interface Sci. 581 (2021) 774–782.
[45] L. Zhang, W. Cai, N. Bao, Adv. Mater. 33 (2021) 2100745.
[46] H. Xu, B. Fei, G. Cai, Y. Ha, J. Liu, H. Jia, J. Zhang, M. Liu, R. Wu, Adv. Energy Mater. 10 (2020) 1902714.
[47] Y. Lan, Y.Y. Liu, J.W. Li, D.J. Chen, G.J. He, I.P. Parkin, Adv. Sci. 8 (2021) 2004036.
[48] T.L. Wang, A. Chutia, D.J.L. Brett, P.R. Shearing, G.J. He, G.L. Chai, I.P. Parkin, Energy Environ. Sci. 14 (2021) 2639–2669.
[49] G.J. He, M. Ling, X.Y. Han, D.I.A.E. Amaiem, Y.L. Shao, Y.M. Li, W.Y. Li, S. Ji, B. Li, Y. Lu, R.J. Zou, F.R. Wang, D.J.L. Brett, Z.X. Guo, C. Blackman, I.P. Parkin, Energy Storage Mater. 9 (2017) 119–125.
[50] S. Li, C. Xi, Y.Z. Jin, D. Wu, J.Q. Wang, T. Liu, H.B. Wang, C.K. Dong, H. Liu, S.A. Kulinich, X.W. Du, ACS Energy Lett. 4 (2019) 1823–1829.
[51] J. Zhang, L. Dai, Angew. Chem. Int. Ed. 55 (2016) 13296–13300.
[52] S.Z. Xu, H.L. Hao, Y.N. Chen, W.Y. Li, W.Z. Shen, P.R. Shearing, D.J.L. Brett, G.J. He, Nanotechnology 32 (2021) 305401.
[53] Y.N. Chen, H.L. Hao, X.K. Lu, W.Y. Li, G.J. He, W.Z. Shen, P.R. Shearing, D.J.L. Brett, Nanotechnology 32 (2021) 195405.
[54] J. Zhang, L. Qu, G. Shi, J. Liu, J. Chen, L. Dai, Angew. Chem. 128 (2016) 2270–2274.
[55] R. Ma, Y. Zhou, Y. Chen, P. Li, Q. Liu, J. Wang, Angew. Chem. Int. Ed. 54 (2015) 14723–14727.
[56] H.S. Jiang, S.Y. Zhao, W.Y. Li, T.P. Neville, I. Akpinar, P.R. Shearing, D.J.L. Brett, G.J. He, Green Energy Environ 5 (2020) 506–512.
[57] N. Zhang, X. Feng, D. Rao, X. Deng, L. Cai, B. Qiu, R. Long, Y. Xiong, Y. Lu, Y. Chai, Nat. Commun. 11 (2020) 4066.
[58] Q. Wang, L. Shang, R. Shi, X. Zhang, Y. Zhao, G.I.N. Waterhouse, L.Z. Wu, C.H. Tung, T. Zhang, Adv. Energy Mater. 7 (2017) 1700467.
[59] S. Gao, Y. Lin, X. Jiao, Y. Sun, Q. Luo, W. Zhang, D. Li, J. Yang, Y. Xie, Nature 529 (2016) 68–71.
[60] C. Liang, P. Zou, A. Nairan, Y. Zhang, J. Liu, K. Liu, S. Hu, F. Kang, H.J. Fan, C. Yang, Energy Environ. Sci. 13 (2020) 86–95.
[61] X. Yu, Z.Y. Yu, X.L. Zhang, Y.R. Zheng, Y. Duan, Q. Gao, R. Wu, B. Sun, M.R. Gao, G. Wang, S.H. Yu, J. Am. Chem. Soc. 141 (2019) 7537–7543.
[62] L. Huang, D. Chen, G. Luo, Y.R. Lu, C. Chen, Y. Zou, C.L. Dong, Y. Li, S. Wang, Adv. Mater. 31 (2019) 1901439.
[63] S. Dresp, F. Dionigi, M. Klingenhof, P. Strasser, ACS Energy Lett. 4 (2019) 933–942.
[64] Y. Kuang, M.J. Kenney, Y. Meng, W.H. Hung, Y. Liu, J.E. Huang, R. Prasanna, P. Li, Y. Li, L. Wang, M.C. Lin, M.D. McGehee, X. Sun, H. Dai, Proc. Natl. Acad. Sci. 116 (2019) 6624–6629.
[65] L. Yu, Q. Zhu, S. Song, B. McElhenny, D. Wang, C. Wu, Z. Qin, J. Bao, Y. Yu, S. Chen, Z. Ren, Nat. Commun. 10 (2019) 5106.

Please cite this article as: J. Wang et al., Mo/Fe bimetallic pyrophosphates derived from Prussian blue analogues for rapid electrocatalytic oxygen evolution, Green Energy & Environment, https://doi.org/10.1016/j.gee.2022.02.014

[66] D.Y. Chung, P.P. Lopes, P. Farinazzo Bergamo Dias Martins, H. He, T. Kawaguchi, P. Zapol, H. You, D. Tripkovic, D. Strmcnik, Y. Zhu, S. Seifert, S. Lee, V.R. Stamenkovic, N.M. Markovic, Nat. Energy 5 (2020) 222–230.
[67] Y. Dou, C.T. He, L. Zhang, H. Yin, M. Al-Mamun, J. Ma, H. Zhao, Nat. Commun. 11 (2020) 1664.
[68] X. Xu, F. Song, X. Hu, Nat. Commun. 7 (2016) 12324.
[69] W. Zhang, H. Song, Y. Cheng, C. Liu, C. Wang, M.A.N. Khan, H. Zhang, J. Liu, C. Yu, L. Wang, J. Li, Adv. Sci. 6 (2019) 1801901.
[70] Z. Chen, B. Fei, M. Hou, X. Yan, M. Chen, H. Qing, R. Wu, Nano Energy 68 (2020) 104371.
[71] J.Y. Xie, Z.Z. Liu, J. Li, L. Feng, M. Yang, Y. Ma, D.P. Liu, L. Wang, Y.M. Chai, B. Dong, J. Energy Chem. 48 (2020) 328–333.
[72] H. Liao, X. Guo, Y. Hou, H. Liang, Z. Zhou, H. Yang, Small 16 (2020) 1905223.
[73] F. Wang, X. Qi, Z. Qin, H. Yang, C. Liu, T. Liang, Int. J. Hydrogen Energy 45 (2020) 13353–13364.
[74] P. Guo, Z. Wang, S. Ge, H. Chen, J. Zhang, H. Wang, S. Liu, S. Wei, X. Lu, ACS Sustain. Chem. Eng. 8 (2020) 4773–4780.
[75] Y. Wang, J. Ma, J. Wang, S. Chen, H. Wang, J. Zhang, Adv. Energy Mater. 9 (2019) 1802939.

Please cite this article as: J. Wang et al., Mo/Fe bimetallic pyrophosphates derived from Prussian blue analogues for rapid electrocatalytic oxygen evolution, Green Energy & Environment, https://doi.org/10.1016/j.gee.2022.02.014